

VIMOS-IFU survey of $z \sim 0.2$ massive galaxy clusters.

I. Observations of the strong lensing cluster Abell 2667^{*}

Giovanni Covone,¹ Jean-Paul Kneib,^{1,2} Geneviève Soucail,³ Johan Richard,³ Eric Jullo¹ and Harald Ebeling⁴

¹ OAMP, Laboratoire d'Astrophysique de Marseille, UMR6110 traverse du Siphon, 13012 Marseille, France

² Caltech-Astronomy, MC105-24, Pasadena, CA 91125, USA

³ Observatoire Midi-Pyrénées, CNRS-UMR5572, 14 Avenue E. Belin, 31400 Toulouse, France

⁴ Institute for Astronomy, University of Hawaii, 2680 Woodlawn Dr, Honolulu, HI 96822, USA

Received —, accepted —.

Abstract We present extensive multi-color imaging and low resolution VIMOS Integral Field Unit (IFU) spectroscopic observations of the X-ray luminous cluster Abell 2667 ($z = 0.233$). An extremely bright giant gravitational arc ($z = 1.0334 \pm 0.0003$) is easily identified as part of a triple image system and other fainter multiple images are also revealed by the *Hubble Space Telescope* Wide Field Planetary Camera-2 images. The VIMOS-IFU observations cover a field of view of $54'' \times 54''$ and enable us to determine the redshift of all galaxies down to $V_{606} = 22.5$. Furthermore, redshifts could be identified for some sources down to $V_{606} = 23.2$. In particular we identify 21 cluster members in the cluster inner region, from which we derive a velocity dispersion of $\sigma = 960^{+190}_{-120} \text{ km s}^{-1}$, corresponding to a total mass of $7.1 \pm 1.8 \times 10^{13} h_{70}^{-1} M_{\odot}$ within a $110 h_{70}^{-1} \text{ kpc}$ (30 arcsec) radius. Using the multiple images constraints and priors on the mass distribution of cluster galaxy halos we construct a detailed lensing mass model leading to a total mass of $2.9 \pm 0.1 \times 10^{13} h_{70}^{-1} M_{\odot}$ within the Einstein radius (16 arcsec). The lensing mass and dynamical mass are in good agreement although the dynamical one is much less accurate. Within a $110 h_{70}^{-1} \text{ kpc}$ radius, we find a rest-frame K-band M/L ratio of $61 \pm 5 h_{70} M_{\odot}/L_{\odot}$. Comparing these measurements with published X-ray analysis, is however less conclusive. Although the X-ray temperature matches the dynamical and lensing estimates, the published NFW mass model derived from the X-ray measurement with its small concentration of $c \sim 3$ can not account for the large Einstein radius observed in this cluster. A larger concentration of ~ 6 would however match the strong lensing measurements. These results are likely reflecting the complex structure of the cluster mass distribution, underlying the importance of panchromatic studies from small to large scale in order to better understand cluster physics.

Key words. Gravitational lensing: strong lensing – Galaxies: clusters – Galaxies: clusters: individual (Abell 2667)

1. Introduction

Massive galaxy clusters are an important laboratory to investigate the evolution and formation of the galaxies and the large scale structure of the Universe (see, e.g., the historical review of the study of galaxy clusters along the last two centuries in Biviano (2000)) and act as natural telescopes magnifying the distant galaxy population. Indeed, the most massive clusters are dense enough to have a central surface mass density larger than the critical density

for strong lensing. This means that multiple images of background sources can be observed, and in some rare cases, when the source position is close to the caustics, highly magnified multiple images can be observed as giant luminous arcs. It is precisely by the observation of this rare events that cluster lensing was discovered (Lynds & Petrosian 1986, Soucail et al. 1987, 1988). Hence, the discovery of a giant luminous arc in a galaxy cluster is a direct evidence for a very dense core, and it also corresponds to a rare opportunity to study in greater details the physical properties of intrinsically faint sources in the high- z Universe as the magnification factor are generally larger than 10 (e.g. Ellis et al. 2001, Kneib et al. 2004a, Kneib et al. 2004b, Egami et al. 2005). On the other hand, using strong and weak lensing in clusters, accurate determination of their mass distribution can be compared to numerical predictions of the Cold Dark Matter scenarios

^{*} Based on observations made with ESO Telescopes at the Paranal Observatories (programs ID 71.A-3010 and 71.A-0428), and on observations made with the NASA/ESA Hubble Space Telescope, obtained from the data archive at the Space Telescope Institute. STScI is operated by the association of Universities for Research in Astronomy, Inc. under the NASA contract NAS 5-26555.

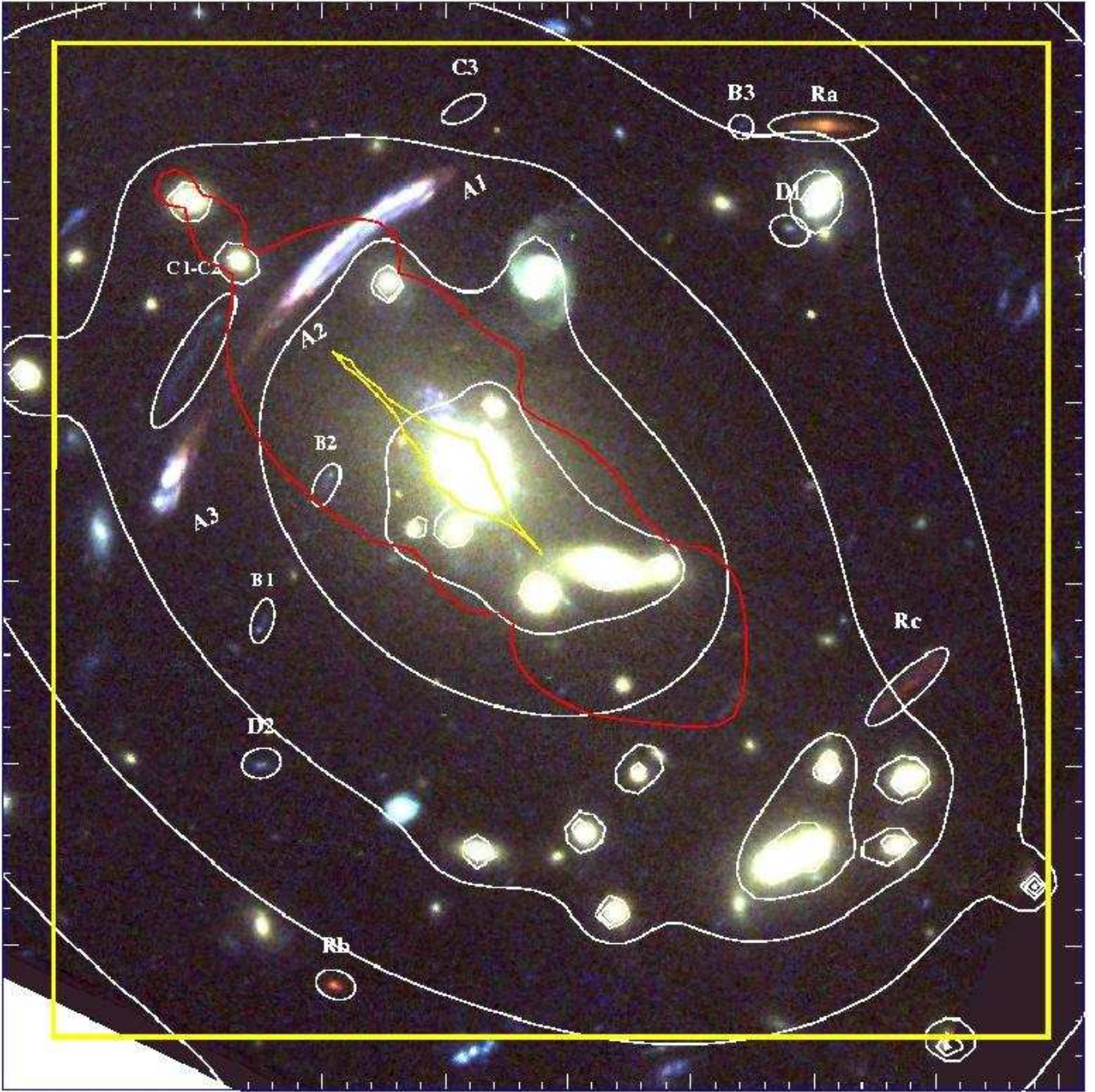


Figure 1. Color image of the Abell 2667 cluster core imaged with HST in the F450W, F606W and F814W filters. The thin yellow square represents the position of the IFU field-of view. Note the strongly magnified gravitational arc and the extended blue region just NE of the central galaxy. The white lines correspond to iso-mass contours from the lens model; the red line is the critical line at the redshift of the giant arc. High- z objects discussed in the text are also marked. North is to the top, East to the Left. The field of view is centered on $\alpha_{J2000}=23:52:28.4$, $\delta_{J2000}=-26:05:08$. At a redshift of $z = 0.233$, the angular scale is 3.722 kpc/arcsec.

(e.g. Kneib et al. 2003, Sand et al. 2004, Broadhurst et al. 2005). In some cases, where multiple images with spectroscopic redshift have been identified in a set of well modeled clusters, it is possible to put significant constraints on the cosmological parameters (Soucail, Kneib & Golse 2004).

Wide field integral field spectroscopy (IFS) is a novel observing technique with straightforward and important applications in the observations of galaxy clusters. Indeed, IFS provides a tool to obtain in an efficient way a complete spectroscopic information in a contiguous sky area, without the multiplexing difficulties of multi-object spec-

troscopy, and, mostly important, without the need of any *a priori* selection of the targets to be observed. For instance, this technique can probe rich clusters at $z \sim 1$ in the early stages of their formation, to obtain a complete (spatially and in magnitude) survey of the galaxy population in the inner and more dense regions.

An important application to massive clusters at intermediate redshift is the survey of the critical lines in the cluster cores to identify gravitationally lensed objects. We have thus started an IFS survey of the critical lines in a sample of eight massive galaxy clusters using the Visible Multi-Object Spectrograph (VIMOS, Le Fèvre et al. 2003) Integral Field Unit (IFU), mounted on VLT Melipal, both in low and high spectral resolution ($R \sim 200$ and 2500, respectively). The cluster sample was selected among X-ray bright, lensing clusters at redshift $z \simeq 0.2$, for which *Hubble Space Telescope* (HST) high-resolution imaging and *Chandra* X-ray observations are already available. The main scientific goals of this project are the search for and the physical characterization of low-mass, highly magnified star forming galaxies (see, e.g., Campusano et al. 2001), the use of strong lensing clusters to constrain the cosmological parameters, as explained by Golse, Kneib & Soucaill (2002) and the study of the evolution of the early-type galaxy population in the rich cluster cores (Covone et al., in preparation).

In this paper, we present the first results from this IFS survey: novel VIMOS-IFU observations and a multi-wavelength imaging analysis of Abell 2667 ($\alpha_{J2000} = 23^h51^m39.4^s$, $\delta_{J2000} = -26^\circ05'02''.8$), a remarkable cluster from the selected sample. In this work we focus on the mass model of this cluster using both strong gravitational lensing and a dynamical analysis of the cluster core; in a forthcoming paper we will present a detailed multi-wavelength analysis of the giant gravitational arc and the other lensed high- z galaxies.

Abell 2667 is a distance class 6, richness class 3 cluster in the Abell catalog (Abell 1958), the cD galaxy being located at redshift $z = 0.233$. Although expected to be an X-ray bright source and to be detected in the ROSAT All-Sky Survey, Abell 2667 is not listed in the X-ray flux limited XBACs sample of Ebeling et al. (1996). The reason for this omission is an unusually large offset of the X-ray position from the optical cluster centroid listed in the Abell catalog. Abell 2667 was then serendipitously detected during ROSAT PSPC observations of the nova-like star V* VZ Scl in December 1992: the X-ray centroid of the cluster was found to be more than $5'$ off the nominal Abell position. It is this X-ray observation of Abell 2667 that has motivated observers to include this object in their optical/X-ray follow-up observations. In particular, a giant luminous arc was easily identified in the cluster core (Rizza et al. 1998; Ebeling et al., in preparation). Remarkably, this arc is so bright that it is detected on DSS2 images (although not recognized as an arc). Using the LRIS spectrograph on the Keck-2 10-m telescope in August 1997 and October 1998, Ebeling et al. (in preparation) obtained long-slit spectra of both knots in the giant arc as well as the third

image. These observations identified the triple arc as a galaxy at a redshift of $z = 1.034 \pm 0.005$ based on a strong [OII] emission line. More recently, a new Keck long-slit optical spectrum of this arc has been obtained by Sand et al. (2005), with the same redshift identification.

Abell 2667 is among the most luminous galaxy clusters known in the X-ray sky: ROSAT HRI observations gave an X-ray luminosity¹ (in the 0.1-2.4 keV band) of $14.90 \pm 0.56 \times 10^{44} h_{70}^{-2} \text{ erg s}^{-1}$ and shows a regular X-ray morphology suggestive of a relaxed dynamical state (Allen et al. 2003). Using the same data, Rizza et al. (1998) estimated a cooling flow time $t_{\text{cool}} = 1.8 \times 10^9$ yrs (much smaller than the age of the Universe at the cluster redshift), and detected the presence of substructure in the intra-cluster medium, as evidenced by the shift of 6.0 ± 2.0 arcsec in the X-ray surface brightness centroid position between the regions in and outside a radius of 150 kpc.

The brightest cluster galaxy is also a powerful radio source, with radio flux density $S = 20.1$ mJy at 1.4 GHz, as measured in the NRAO VLA Sky survey (Condon et al. 1998). This galaxy was also included in the sample of radio emitting X-ray sources observed by Caccianiga et al. (2000). They found strong optical nebular emission lines and classified this source as a narrow emission line AGN (i.e., all the observed emission lines have FWHM lower than 1000 km s^{-1} in the source rest frame). More recently, Allen et al. (2003) have used *Chandra* data to estimate the mass of this cluster: by fitting a Navarro-Frenk-White (1996; NFW) model, they have found, within a virial radius of r_{200} , $M_{200} = 13.6^{+10.6}_{-4.6} 10^{14} h_{70}^{-1} M_{\odot}$, with a concentration $c = 3.0 \pm 0.8$. Fukazawa et al. (2004) have measured an X-ray temperature of 6.15 ± 0.61 keV (excluding the central cool region), based on ASCA observations. Using archive ROSAT and ASCA, Ota & Mitsuda (2004) have obtained a new measurement of the X-ray temperature, found to be $5.95^{+0.42}_{-0.23}$ keV.

The outline of the paper is the following. We present the IFU observations in Sect. 2 along with the other supporting imaging observations. The IFU data reduction and analysis is presented in Sect. 3. Sect. 4 presents the catalog and the spectroscopic information derived from the IFU data; Sect. 5 the lensing and dynamical mass models are discussed and compared with recent mass estimates based on X-ray observations. Finally, the main results are summarized in Sect. 7. In the following, magnitudes are given in the AB system.

2. Observations

2.1. Imaging data

Abell 2667 was observed on October 10-11, 2001 with the *HST* using the WFPC2 in the F450W (5x2400 s), F606W

¹ Throughout this paper we will assume a cosmological model with $\Omega_m = 0.3$, $\Omega_{\Lambda} = 0.7$ and $H_0 = 70 h_{70} \text{ km s}^{-1} \text{ Mpc}^{-1}$. At $z = 0.233$ the angular scale is thus $3.722 \text{ kpc arcsec}^{-1}$.

(4x1000 s) and F814W (4x1000 s) filters (PI: Allen, proposal ID: 8882). Images have been retrieved from the ST-ECF archive and reduced using the IRAF *drizzle* package (Fruchter & Hook 2002). The final spatial resolution of the images is $0''.05$ per pixel. Fig. 1 shows a color image of the cluster core made of the 3 *HST* images: the giant luminous arc is very prominent, and other new candidate multiple images systems (see discussion in Sect. 5) are indicated. The 5σ limit detection for point sources on the final images is 24.76, 25.44 and 24.61 in the filters F450W, F606W and F814W, respectively.

On 30 May and 1st June 2003 near-infrared J and H-band observations with ISAAC have been obtained with the *Very Large Telescope* (VLT) (as part of program ID: 71.A-0428, PI: Kneib), under photometric sky conditions. The total exposure time for the J-band and H-band ISAAC data are 7932 s ($34.8 \times 4 \times 57$ s) and 6529 s ($11.4 \times 10 \times 57$ s), respectively. The data were reduced using standard IRAF scripts: the final seeing is $0''.51$ and $0''.58$ in the J-band and in the H-band, respectively (pixel scale is $0''.148$ per pixel). The measured 5σ detection limit for point sources are respectively 25.6 and 24.7 in J and H, respectively.

2.2. VIMOS-IFU 3D spectroscopy

The integral field spectrograph is one of the three operational modes available on VIMOS (Le Fèvre et al. 2003). The IFU consists of 4 quadrants of 1600 fibers each, feeding four different $2k \times 4k$ CDDs. Each quadrant is made by four sets (*pseudo-slits*) of 400 fibers. Up to date, the VIMOS-IFU is the integral field spectrograph with the largest field of view (f.o.v.), among those available on 8/10-m class telescopes: the f.o.v. covers (in the lower spatial resolution mode) a contiguous sky region of $54'' \times 54''$, with 6400 fibers of $0''.66$ diameter. The dead space between adjacent fibers is less than 10 % of the fiber dimension.

The galaxy cluster Abell 2667 has been observed in service mode on the nights 29 and 30 June 2003 (as part of program ID: 71.A-3010, PI: Soucail). Both nights were photometric, with the DIMM seeing varying between $0''.6$ and $0''.8$ during the observations of the cluster, performed at airmass always lower than 1.28. We have used the spatial low-resolution mode (fibers with diameter $0''.66$), and the low-resolution blue grism (LR-B) in combination with an order sorting filter, which covers the wavelength range from 3500 Å to 7000 with spectral resolution $R \sim 250$ and dispersion 5.355 Å/pixel. However, because of the overlapping of the spectra between contiguous pseudo-slits on the CCD, the first and last $\simeq 50$ pixels on the raw spectra from most of the pseudo-slits are not usable. This reduces the useful spectral range approximatively from 3900 to 6800 Å.

The overall exposure time is 10.8 ksec (4×2700 s, two exposures were obtained each night). A small offset of about 2 arcsec among consecutive exposures has been

applied, in order to compensate for the effect due to the not uniform efficiency of the fibers and the presence of a small set of low quality fibers.

Calibration frames have been obtained soon after each one of the 4 exposures and a spectrophotometric standard star has been observed each night. The final area is $54''.8 \times 55''.4$, corresponding to a region of about 200×200 kpc², centered $5''$ SW from the brightest cluster galaxy.

3. Reduction of the VIMOS-IFU data

The whole reduction process of the VIMOS-IFU data has been completed using the VIMOS Interactive Pipeline Graphical Interface (VIPGI, Scodreggio et al. 2005), a dedicate tool to handle and reduce VIMOS data². See also Zanichelli et al. (2005) for a description of the data reduction methods and the quality assessment. Every reduction step before the final combination of the dithered exposures in a single data cube is performed on a single quadrant basis. The main steps are the followings: check and adjustment of the so-called *first guesses* of the instrumental model (see later on), creation of the spectra extraction tables at each pointing, CCD preprocessing, wavelength calibration, cosmic ray hits removal, determination of fiber efficiency, sky background subtraction and flux calibration.

The VIMOS-IFU data reduction requires a highly accurate description of the optical and spectral distortions of the instrument, especially for the spectra location and the wavelength calibration. These distortions are modeled using third order polynomials, whose coefficients (as periodically determined by the staff at the telescope) are stored in the raw FITS files headers. However, since these distortions may change in time (because of, e.g., the different orientation of the instrument during observation or the instrument aging) such a predefined model can only be used as a first guess when calibrating the scientific frames. Moreover, we have experienced that most of the times these first guesses are not close enough to the actual instrument distortions to be safely used, mainly because of the large flexures of the instrument between the time of their definition and the time of observation (see, e.g., D’Odorico et al. 2003). These can sum up to a few pixels (see, e.g., D’Odorico et al. 2003), and are larger for observations at the meridian and close to the zenith, like in the present case. Therefore, the original first guesses for the spectra location and the inverse dispersion law need to be checked and corrected for any given pointing, by using the calibration frames as close in time as possible to the scientific exposures and taken at the same rotator absolute position. At this aim, we used a specific graphically guided tool provided by VIPGI to correct interactively the polynomial coefficients describing the optical and wavelength distortions (Scodreggio et al. 2005), independently for each

² VIPGI has been developed within the VIRMOS Consortium. See the VIPGI web site for more information: <http://cosmos.mi.iasf.cnr.it/marcos/vipgi/vipgi.html>

calibration set associated to the scientific exposures. These corrected values are then used in the following location of spectra traces and wavelength calibration.

Having adjusted the first guesses for the optical distortions, it is then possible to trace the spectra of the 4 detectors. Location of the spectra traces is a very critical step, since spectra are highly packed on the CCDs: distances between spectra from contiguous fibers is 5 pixels, each fiber having a FWHM of $\simeq 3.2$ pixels. Therefore, even small errors (~ 1 pixel) in tracing the exact position of the spectra can result in a degraded quality of the final result. Because of their high S/N, we have used flat field lamps taken immediately after each science exposure to trace the spectra. In this step an extraction table is created, which is then used to trace spectra of the scientific exposures. The accuracy of the extraction tables has been visually checked on the raw science frame themselves, by verifying that the fibers with highest signal are indeed correctly traced.

Because of the high density of the spectra on the VIMOS detectors, there is a not negligible amount of crosstalk, i.e., flux contamination among nearby fibers. However, we have done no attempt to correct for this effect: indeed, correcting for the cross-talk would need a very good modeling of the fibers profile in the cross-dispersion direction. Zanichelli et al. (2005) have shown that the average contamination on each neighboring fiber is $\sim 5\%$, i.e. smaller or of the same order of magnitude of the error introduced by fitting the fibers profile, since the quality of crosstalk correction decreases rapidly as soon as the error on the width measurements is of the order of $\simeq 0.2$ pixels.

The inverse dispersion law is calculated starting from the adjusted first guesses and a fit by a third order polynomial function. All the inverse dispersion solutions have been visually checked, by comparing the predicted positions of arc lamp lines (Neon and Helium lamps) with their effective positions on raw frames. To demonstrate the accuracy of the wavelength calibration, in Fig. 2 the distribution of the RMS residuals in the wavelength calibration for the 6400 fibers in a single pointing is plotted: the median values is 0.716 \AA , i.e. about 0.15 pixels, with negligible differences among the four quadrants.

The scientific exposures have been overscan trimmed and bias subtracted, and cosmic ray hits have been cleaned. The cleaning algorithm (described in Zanichelli et al. 2005) is based on a sigma-clipping method and the fact that along the dispersion direction also spectra with strong emission lines show a smooth behavior, while comets rays show very strong gradients. This method is very efficient in removing hits spanning only a few pixels ($\sim 99\%$), and has lower efficiency ($\sim 90\%$) just in the case of more extended ones. A further cleaning has therefore been applied in the final combination of the dithered exposures.

Finally, the wavelength calibration is applied and the 1D-spectra are extracted. Extraction of the spectra is based on the Horne's (1986) recipe. At this stage sky lines are used to check and refine the wavelength calibration, in

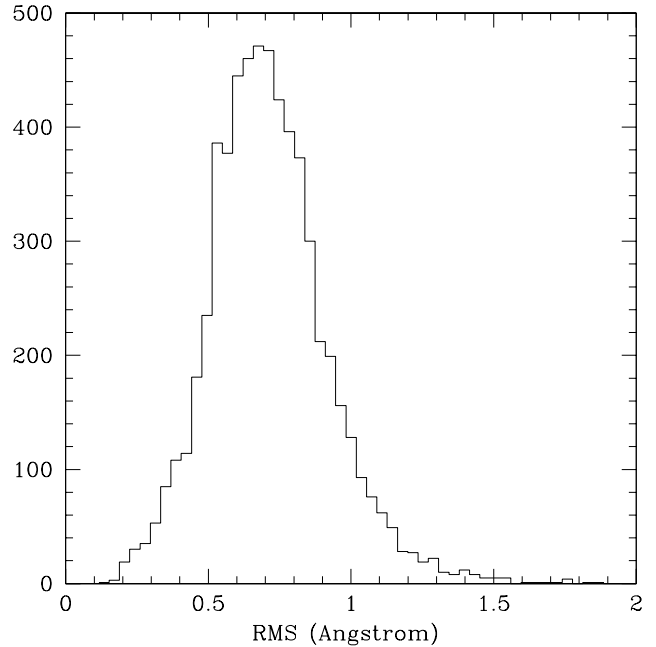


Figure 2. Distribution of the RMS residuals in the wavelength calibration for all the useful fibers in the first pointing. The median value is 0.716 \AA , i.e. 0.15 pixel. 95% of the fiber has RMS lower than 1.0 \AA .

order to compensate the effects of possible further differential flexures between the lamp and scientific exposures.

Then, the correction of the fiber-to-fiber relative transmission (analogous to the flat-fielding in the imaging case) is done by measuring in each 1D spectrum the flux contained in an user specified strong sky line, either the 5577 \AA or the 5892 \AA lines. We have calculated the relative transmission of each fiber independently in 16 different exposures with the given grism performed in the present observing run, and used its median value.

Since VIMOS-IFU has not a dedicated set of fibers to determine the sky background level, sky subtraction is performed in a statistical way: in each module, fibers are grouped in three sets according to their shape (as characterized by the FWHM and skewness of the fiber output on the CCD), and the sky level is obtained by their mode (Scodeggio et al. 2005). This approach gives robust results when applied to a field in which most of the fibers have only sky signal, like in the present case.

Flux calibration is done separately for each quadrant of the single exposures, using the observations of a standard star. A sequence of observations with the star centered respectively on each quadrant is taken each night. From the comparison of the flux-calibrated spectra with the B_{450} and V_{606} magnitudes, we estimated the accuracy of the spectrophotometric calibration to be $\sim 20\%$.

Finally, the four fully reduced exposures have been combined together, by using shifts of integer number of fibers. The final data cube has been corrected for the effect due to the differential atmospheric refraction using

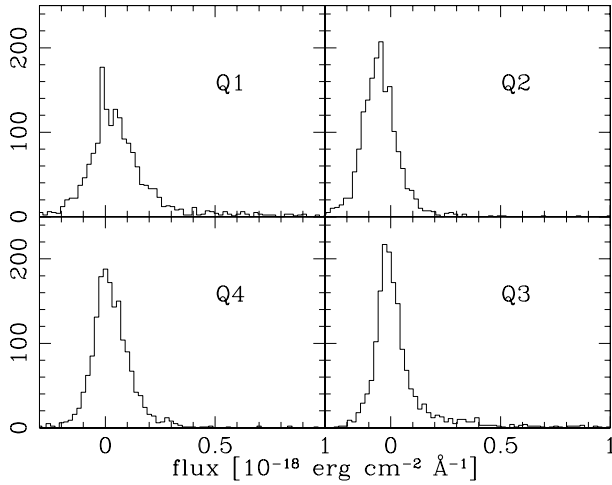


Figure 3. Distribution of the average fibers flux values between 4000 and 6200 Å in the four quadrants of the fully reduced datacube, showing the uniformity of the background in the different quadrants. In all quadrants, distributions are centered around zero, with standard deviation $0.7 - 1.1 \times 10^{18} \text{ erg cm}^{-2} \text{ Å}^{-1} \text{ s}^{-1}$.

the formula from Filippenko (1982) and converted to the Euro3D FITS data format (Kissler-Patig et al. 2004).

The final data cube is made of 6806 spatial elements, each one representing a spectrum going from $\simeq 3900$ to 6800 Å ; it covers a sky area of 0.83 arcmin^2 , centered $5''$ arcsec South-West of the brightest cluster galaxy. The median spectral resolution is $\simeq 18 \text{ Å}$, as estimated from Gaussian fits to sky lines in the final datacube. The 3D-cube has been explored and analyzed by using the visualization tool E3D (Sánchez 2004) and specific IDL programs written by the authors. In Fig. 3 we plot the average flux distribution of all the 6806 spatial elements of the final data-cube: globally, the four IFU quadrant show a good uniformity in terms of sky background level and noise, the flux distribution being very well described by a Gaussian peaked around zero, with a small tail representing the fibers located on detected objects. The overall sky background subtraction is relatively accurate, as the background level in the final datacube is around zero in the blank sky regions at all wavelengths. However, the root-mean-square fluctuations of the background are a strong function of the sky position and the wavelength, as further discussed in Sect. A. Finally, a major limitation above $\sim 6200 \text{ Å}$ is given by the zero order contaminations, whose position changes from one pseudo-slit to the other and from quadrant to quadrant.

A bi-dimensional color projection of the data-cube is shown in Fig. 4. In this image, the blue, green and red color channels have been built by averaging the flux in the following spectral ranges: $4500\text{--}4700 \text{ Å}$ (therefore including the [OII] emission line at the cluster redshift), $4900\text{--}5400 \text{ Å}$, (which covers the 4000 Å break at the cluster redshift), and $5700\text{--}6200 \text{ Å}$. The giant arc, which is characterized by a strong continuum emission, is remarkable at all wave-

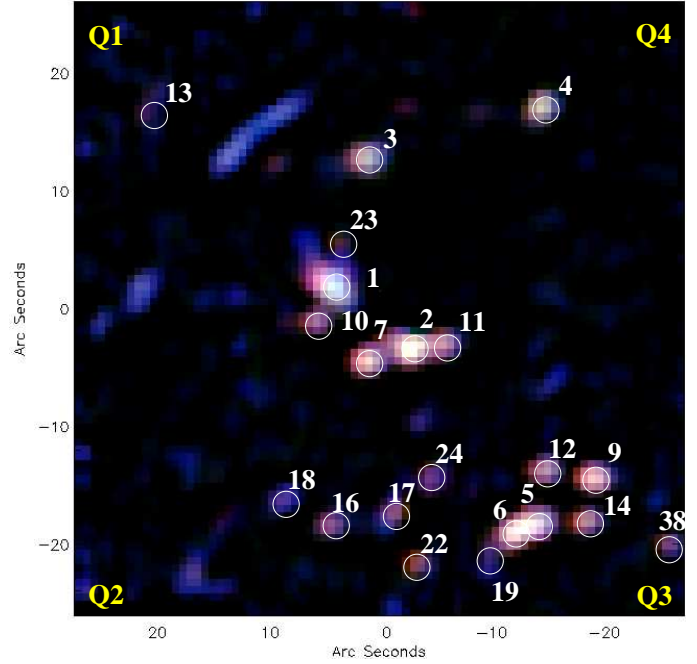


Figure 4. VIMOS-IFU bi-dimensional color image of the central region of the cluster Abell 2667. The blue, green and red color channels have been built by averaging the flux in the spectral ranges: $4500\text{--}4700 \text{ Å}$, $4900\text{--}5400 \text{ Å}$ and $5700\text{--}6200 \text{ Å}$, respectively. Same orientation as in Fig. 1. The blue region just NE of the cD galaxy corresponds to an extended emission line region at the same redshift of the cD. The 21 galaxies with secure redshift measurement (excluding the lensed sources A and Ra) are identified in the plot.

lengths, and also the blue emitting region around the central galaxy and the brightest cluster galaxies are easily recognized.

4. The catalog

The photometric catalog of objects within the VIMOS-IFU field of view has been built using SExtractor (Bertin & Arnouts 1996) on the χ^2 -image obtained by combining the HST F450W- and F606W-band images (which overlap the spectral range of the VIMOS-IFU data). We have used the Skycat GAIA tool to find the astrometric solution for the IFU data-cube in order to identify the fibers covering the detected objects. For each object a 1D spectrum is obtained by summing the signal on all the associated fibers. We have also searched directly the VIMOS-IFU datacube for objects using a dedicate tool prepared by the authors (Covone et al., in preparation). One bright object (ID = 38) has been detected in the IFU datacube and has no HST counterpart since this falls outside of the WFPC2 f.o.v. Finally, $N=39$ objects have been detected in the VIMOS-IFU data cube, an object being considered as detected if we could find at least a featureless continuum at the position of the HST object.

Table 1. Spectrophotometric catalog of the galaxies, within the VIMOS-IFU f.o.v. Columns 4 and 7 list the total magnitudes B_{450} and J (AB system), while colors are measured on $2''$ apertures. Flag represents quality of the redshift measurements (see text). In the last column, we specify the type of spectral features identified in the spectra.

ID	$\alpha(J2000)$	$\delta(J2000)$	B_{450}	B-V	B-I	J	J-H	z	flag	lines
1	23:51:39.4	-26:05:03.3	19.12	1.03	1.90	16.58	0.25	0.2348	4	abs, em
2	23:51:38.8	-26:05:08.8	20.34	1.56	2.33	17.32	0.21	0.2465	4	abs
3	23:51:39.1	-26:04:52.8	20.64	1.14	1.66	18.49	0.13	0.2233	4	abs
4	23:51:38.0	-26:04:48.2	20.90	1.24	1.89	18.43	0.14	0.1570	4	abs
5	23:51:38.0	-26:05:24.0	20.90	1.53	2.27	17.94	0.19	0.2346	4	abs
6	23:51:38.2	-26:05:24.8	20.93	1.47	2.20	18.00	0.19	0.2316	4	abs
7	23:51:39.1	-26:05:10.2	20.97	1.60	2.39	17.85	0.23	0.2316	4	abs
8	23:51:39.7	-26:04:53.2	21.06	1.31	1.97	18.73	0.10	0.2205	1	abs
9	23:51:37.6	-26:05:20.0	21.53	1.54	2.32	18.45	0.21	0.2338	4	abs
10	23:51:39.5	-26:05:06.8	21.73	1.47	2.21	18.79	0.20	0.2353	4	abs
11	23:51:38.6	-26:05:08.6	21.82	1.55	2.29	18.87	0.20	0.2309	4	abs
12	23:51:38.0	-26:05:19.4	21.86	1.56	2.31	18.73	0.21	0.2311	4	abs
13	23:51:40.6	-26:04:48.8	21.89	1.46	2.23	19.00	0.20	0.2333	2	abs
14	23:51:37.7	-26:05:23.8	21.94	1.51	2.27	18.94	0.19	0.2325	4	abs
15	23:51:40.3	-26:04:52.1	21.98	1.39	2.10	19.20	0.13	—	—	—
16	23:51:39.4	-26:05:24.4	22.16	1.40	2.12	19.39	0.17	0.2447	2	abs
17	23:51:38.9	-26:05:23.3	22.22	1.43	2.12	19.44	0.15	0.2308	4	abs
18	23:51:39.7	-26:05:22.1	22.29	0.82	1.18	20.78	0.04	0.3980	3	em
19	23:51:38.3	-26:05:27.0	22.38	1.31	1.95	19.70	0.17	0.2290	2	abs
20	23:51:39.6	-26:05:06.7	22.48	1.48	2.20	19.64	0.20	0.2404	1	abs
21	23:51:40.9	-26:05:07.1	22.55	0.86	1.29	21.11	0.06	0.2140	1	abs, em
22	23:51:38.8	-26:05:27.6	22.60	1.60	2.37	19.47	0.22	0.2352	4	abs
23	23:51:39.3	-26:04:59.9	22.66	1.43	2.18	19.82	0.20	0.2360	3	abs, em
24	23:51:38.7	-26:05:20.0	22.94	1.50	2.23	19.98	0.18	0.2351	4	abs
25	23:51:40.2	-26:05:28.6	23.04	1.32	2.02	20.54	0.14	0.2255	1	abs
26	23:51:38.0	-26:04:50.1	23.40	1.10	1.73	21.04	0.14	—	—	—
27	23:51:37.1	-26:04:53.9	23.53	0.30	0.80	21.84	0.17	—	—	—
28	23:51:38.4	-26:04:48.6	23.58	1.19	1.88	21.27	0.07	0.2440	1	abs
29	23:51:39.1	-26:04:39.0	23.59	0.25	0.58	22.12	0.14	—	—	—
30	23:51:38.8	-26:05:15.1	23.77	1.51	2.19	20.96	0.12	0.2336	1	abs
31	23:51:39.3	-26:05:35.2	23.87	0.19	0.16	22.90	-0.23	—	—	—
32	23:51:41.0	-26:04:50.0	23.89	0.23	0.48	22.66	-0.44	—	—	—
33	23:51:39.7	-26:05:01.9	23.91	1.39	2.58	20.41	0.05	0.2380	1	abs
34	23:51:38.0	-26:04:54.6	24.28	0.69	0.99	23.58	-0.02	—	1	—
35	23:51:39.0	-26:05:24.6	24.51	1.42	2.19	21.46	0.10	0.2270	1	abs
36	23:51:37.3	-26:04:53.7	24.56	0.15	0.40	23.68	-0.33	—	—	—
37	23:51:40.8	-26:05:19.5	24.81	1.10	1.58	23.22	-0.09	—	—	—
38	23:51:37.1	-26:05:25.3	—	—	—	19.81	0.20	0.2301	3	abs

The redshifts have been measured using a cross-correlation technique by means of the IRAF task `xcsao` (Kurtz et al. 1992), and attentively visually checked by at least two of us. The median error on individual measurements, as estimated by using this software, is ~ 0.0003 . The instrumental uncertainty is about $\sim 100 \text{ km s}^{-1}$ in the rest frame. We assigned a confidence class from 1 to 4, following Le Fèvre et al. (1995): class 1 corresponds to a subjective probability of 50 % that the lines identification is correct, class 2 to a probability of 75 % (with more than one spectral feature identified), class 3 to a probability higher than 95% and class 4 to an unquestionable identification.

We have obtained redshift measurements for 34 objects, including 25 secure ones (i.e., confidence class higher

than 1). The faintest object for which we could measure the redshift has magnitude $B_{450} = 24.58$ (in a $2''$ aperture). The final galaxy catalog is shown in Table 1, while information on the gravitationally lensed sources is given in Table 2. Table 1 contains photometric and spectroscopic information for the objects with a redshift measurement, and photometric information for the remaining objects brighter than $B_{450} = 24.8$.

The overall efficiency of the redshift survey within the central region of A2667 is plotted in Fig. 5. We could measure the spectroscopic redshifts for all galaxies brighter than $B_{450} \simeq 23.0$, apart for object #15, which is located in a region covered by dead fibers. The redshift survey is complete down to $V_{606} \sim 22.5$, where we could determine redshifts for about half of the objects in the f.o.v. In Fig. 6

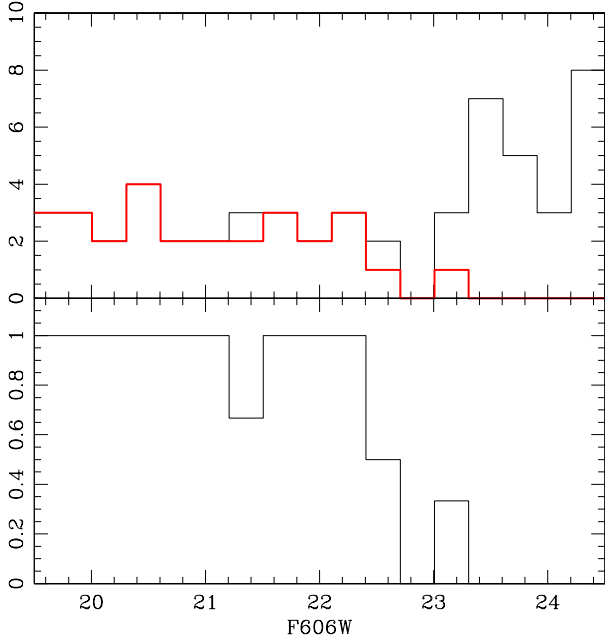


Figure 5. Completeness of redshift survey as function of V-band magnitude (measured in a $2''$ aperture). In the upper panel, we plot the number of objects detected on the HST χ^2 -image within the VIMOS-IFU f.o.v. (black line), and the number of those object with measured redshift (red line). In the lower panel, the efficiency of the spectroscopic survey is given. The redshift of bright object at $V \simeq 21.5$ (ID=15) was not measured since it is located on a set of dead fibers.

we plot the color-magnitude diagram for all the objects within the VIMOS-IFU f.o.v. detected on the HST data. Redshifts could be measured for almost all the galaxies belonging to the cluster red sequence.

27 galaxies fall in the redshift range $0.21 < z < 0.25$ (including all measurement flags). We used a classical bi-weight distribution method (Beers et al. 1990) to determine the cluster membership and velocity dispersion. Considering 22 galaxies as belonging to the cluster core, we derive a cluster redshift of $z_{cl} = 0.233 \pm 0.003$ (i.e., the median redshift of the assumed cluster members) and a velocity dispersion of $\sigma_{cl} = 960^{+190}_{-120} \text{ km s}^{-1}$. The redshift distribution of galaxies in the range $0.21 < z < 0.25$ is shown in Fig. 7. The cD galaxy redshift is $z = 0.2348 \pm 0.0002$, which within the uncertainty is consistent with being at rest in the cluster potential well.

All cluster galaxies show the typical features of evolved early-type galaxies (a red continuum with strong absorption lines characteristic of an evolved stellar population), as expected in the central region of a relaxed cluster. Four representative spectra of cluster members are plotted in Fig. 8. The largest majority of the cluster member shows no strong nebular emission line possibly associated with on-going star formation, except the cD galaxy which has a rich and spatially extended structure of strong emission

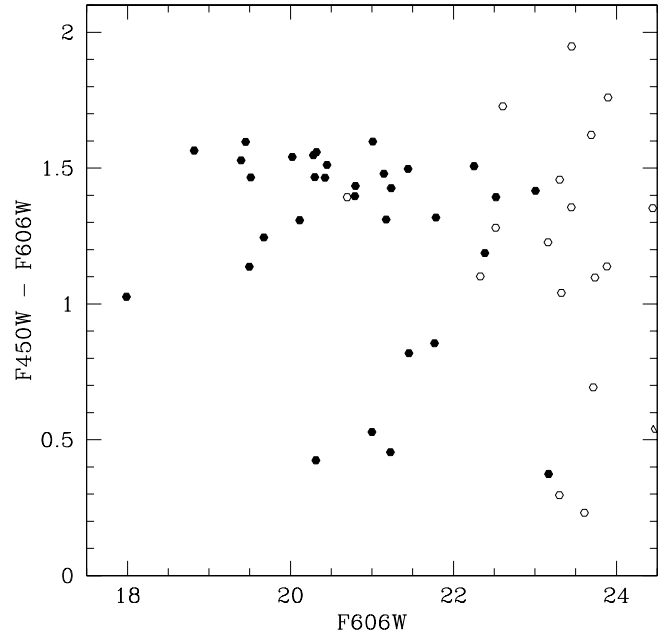


Figure 6. Color-magnitude relation of the galaxies in VIMOS-IFU f.o.v and detected in the HST χ^2 -image, using the two WFPC2 pass-bands covering the LR-B spectral range (F450W and F606W). Filled symbols correspond to objects with measured redshift, empty symbols to objects with no redshift measurement. The cD galaxy (ID=1) is the brightest object in the diagram, out of the color-magnitude relation because of the blue excess associated with the extended emission line region.

lines. In particular, the associated [OII] emission line extends well beyond the galaxy itself (see the blue region visible in Fig. 1 and Fig. 4), also where the red continuum of the evolved stellar population is barely detected. Further investigation of this spatially extended emission and the cluster galaxies population will be presented in a forthcoming paper.

In Fig. 9 we show the spectra of the three images A1, A2 and A3 forming the giant gravitational arc. The source is a blue star-forming galaxy at redshift 1.0334 ± 0.0003 , whose spectrum is characterized by a bright continuum with strong UV absorption lines (FeII and MgII), thus confirming the initial spectroscopic identification of the [OII] emission line by Ebeling et al. (in preparation), see also Sand et al. (2005).

In Fig. 1 three relatively red, physically unrelated, objects are visible: Ra, Rb, Rc. They are not detected in the B₄₅₀ image but clearly visible in the redder broad-band images. They are background galaxies slightly magnified by the cluster gravitational field.

The spectrum of the object Ra (see Fig. 10) shows a weak red continuum at wavelengths $\lambda \gtrsim 6000 \text{ \AA}$: the possible identification of the 4000 \AA break and the overall shape of the continuum lead to a redshift measurement of

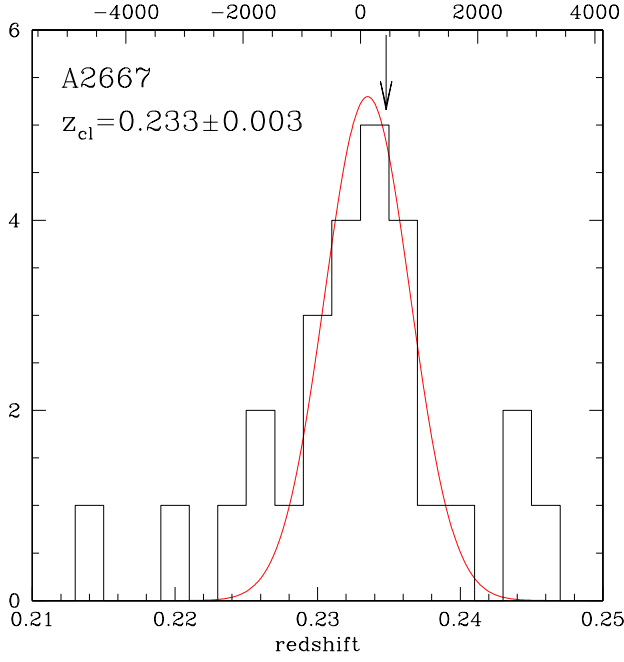


Figure 7. Redshift distribution of galaxies in the vicinity of the cluster. The bulk of galaxies are bounded to the cluster centered at $z = 0.233$ with a velocity dispersion of 960 km s^{-1} (overlaid Gaussian profile). The arrow marks the position of the central galaxy. Bin size is $\Delta z = 0.002$; on the top axis velocities relative to the cluster rest frame are shown (in km s^{-1}).

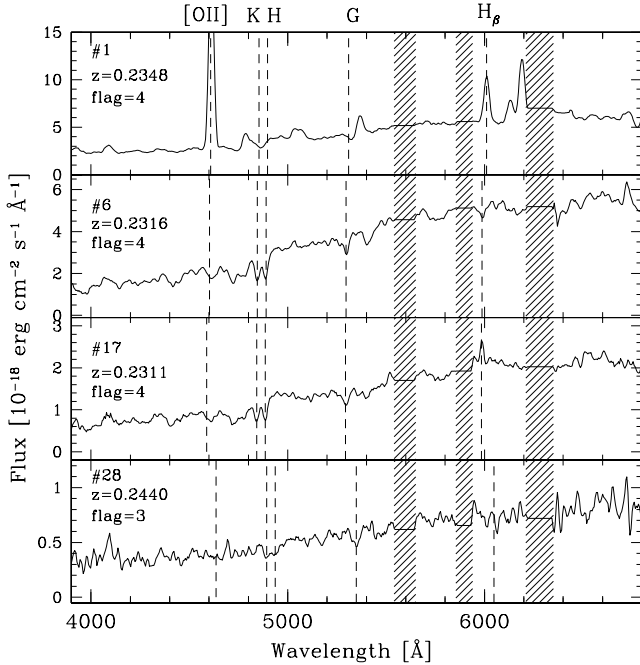


Figure 8. Four representative spectra of cluster members from the VIMOS-IFU survey of A2667 core, in order of decreasing luminosity. Only a few of the detected lines are indicated. Spectra have been smoothed at the instrumental resolution. Shaded region are strongly affected by sky lines residuals.

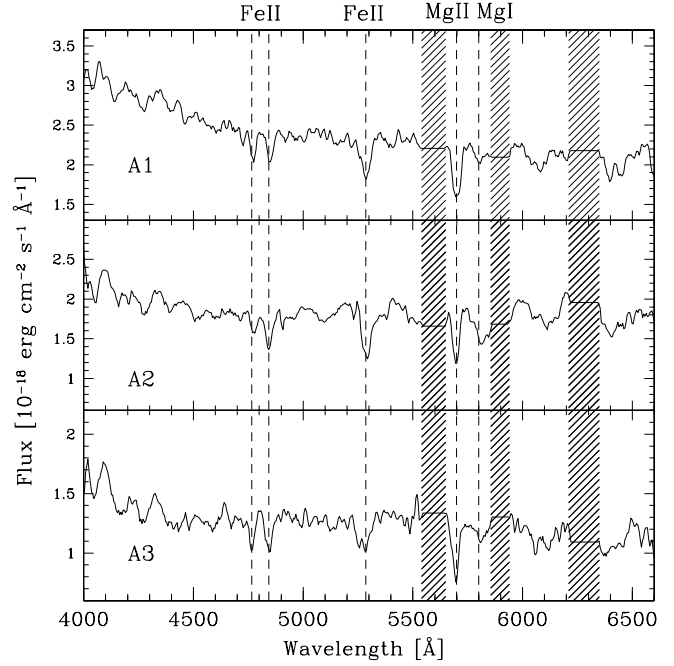


Figure 9. VIMOS-IFU spectra of the three giant arc components. Individual spectra are obtained by averaging the flux of the fibers at the images positions. Spectra have been box-car smoothed. Vertical lines show the position of the identified UV absorption features. The redshift of the source is $z_{\text{arc}} = 1.0334$. Shaded regions mark the spectral ranges dominated by sky-lines residuals.

$z = 0.620$. The absence of a lensed counterparts allows to put a firm upper limit of $z \simeq 3.5$.

At the expected position in the VIMOS-IFU data-cube of the other two red objects (Rb and Rc), the continuum at $\lambda \gtrsim 6300 \text{ Å}$ is too noisy to identify unambiguously any spectral feature. The absence of lensed counterparts puts an upper limit to Rc ($z < 1.5$), while Rb is not expected to be multiply imaged at any redshift location.

5. Mass models

5.1. The lensing mass model and multiple images redshift prediction

To model the mass distribution of this cluster we used both a cluster mass-scale component (representing the contribution of the dark matter halo and the intra-cluster medium) and cluster galaxy mass components in a similar way to Kneib et al. (1996), see also Smith et al. (2005). Cluster galaxies have been selected according to their redshift (when available, in the inner cluster region covered with VIMOS spectroscopy) or their J-H color, considering galaxies belonging to the cluster red sequence. We also included the lensing contribution from the foreground galaxy #3 ($z = 0.1570 \pm 0.0002$), rescaling its lensing properties at the cluster redshift. In total, the mass distribution model is made of 70 mass components, including the large scale cluster halo and the individual galaxies.

Table 2. Properties of the lensed systems and red background galaxies magnified by the galaxy cluster. In the redshift column we list the spectroscopic redshift (if measured) or the photometric one. In the last column, the flag of the spectroscopic redshift or the predictions z_{mod} (or the constraints on the redshift) from the strong lensing model are given. Spectroscopic redshifts are obtained by summing all the images in the given lensed system.

ID	$\alpha(\text{J2000})$	$\delta(\text{J2000})$	B_{450}	redshift	notes
<i>multiple images system</i>					
A1	23:51:39.7	-26:04:48.8	20.26	1.0334 ± 0.0003	flag=4
A2	23:51:40.0	-26:04:52.0	20.62	1.0334 ± 0.0003	flag=4
A3	23:51:40.6	-26:05:04.0	21.30	1.0334 ± 0.0003	flag=4
B1	23:51:40.3	-26:05:12.0	25.13	$z_{\text{ph}} = 1.20 \pm 0.12$	$z_{\text{mod}} = 1.25 \pm 0.05$
B2	23:51:40.0	-26:05:03.5	23.13	–	$z_{\text{mod}} = 1.25 \pm 0.05$
B3	23:51:38.3	-26:04:44.3	25.99	–	$z_{\text{mod}} = 1.25 \pm 0.05$
C1	23:51:40.6	-26:04:56.0	24.95	1.578 ± 0.004	flag=1, $z_{\text{mod}} = 1.6 \pm 0.1$
C2	23:51:40.7	-26:04:59.1	24.86	1.578 ± 0.004	flag=1, $z_{\text{mod}} = 1.6 \pm 0.1$
D1	23:51:38.1	-26:04:49.8	24.29	$z_{\text{ph}} = 3.12 \pm 0.10$	$z_{\text{mod}} = 3.2 \pm 0.2$
D2	23:51:40.3	-26:05:19.4	25.09	$z_{\text{ph}} = 2.85 \pm 0.10$	$z_{\text{mod}} = 3.2 \pm 0.2$
<i>single image systems</i>					
Ra	23:51:39.4	-26:05:03.3	23.90	0.620 ± 0.003	flag=1
Rb	23:51:40.0	-26:05:31.5	27.09	$z_{\text{ph}} = 0.95 \pm 0.05$	–
Rc	23:51:37.6	-26:05:14.8	23.74	$z_{\text{ph}} = 1.15 \pm 0.05$	$z_{\text{mod}} < 1.5$

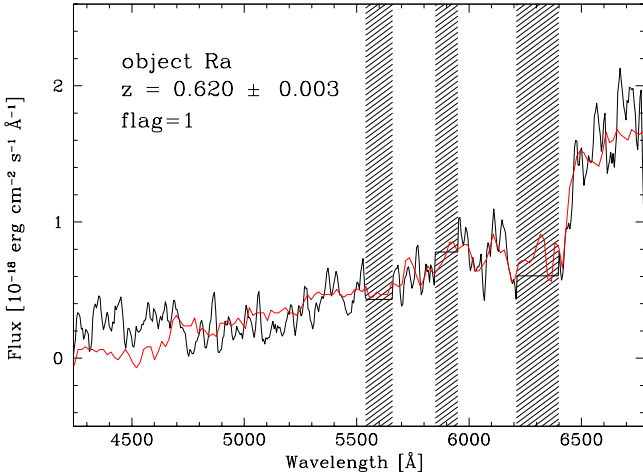


Figure 10. VIMOS-IFU spectrum of the red object Ra (black line, smoothed at the instrumental resolution), together with a redshifted spectrum of a local early-type galaxy (red line). The spectroscopic redshift is based mainly on the identification of the 4000 Å break.

We included in the mass model all the cluster galaxies brighter than $\simeq 0.05 L_{\text{H}}^*$, a luminosity limit at which their additional contribution is comparable with uncertainties in the overall cluster model. All model components have been parameterized using a smoothly truncated pseudo-isothermal mass distribution model (PIEMD, Kassiola & Kovner 1993), which avoids the unphysical central singularity and infinite spatial extent of the singular isothermal model.

The galaxy mass components have been chosen to have the same position, ellipticity and orientation as of

their corresponding H-band image. Their mass has been scaled with their estimated K-band luminosity, assuming a Faber-Jackson (1976) relation and a global mass-to-light ratio (M/L) which is independent of the galaxy luminosity (see Appendix in Smith et al. 2005). In short, the K-band luminosity is computed, assuming a typical E/S0 spectral energy distribution (redshifted but not corrected for evolution) for the selected cluster galaxies. Moreover, we also used a model in which the mass-to-light ratio has a weak dependence on the luminosity, $M/L \propto L^{0.3}$, as implied by the Fundamental Plane (Jorgensen et al. 1996, see also Natarajan & Kneib 1997).

Using the `lenstool` ray-tracing code (Kneib 1993), we iteratively implemented the constraints from the gravitational lenses: we started by including the triple imaged giant luminous arc A1,2,3. The high-resolution HST images show a clear mirror symmetry along this giant arc (fold arc) which gives additional constraints on the location of the critical line at the main arc redshift. Then we used the predictions of the lensing model to find additional lensed systems and include their constraints to improve the model. In particular, we used the position and the morphology of the following fainter multiple images: B1, B2, B3; C1, C2, C3 and D1, D2 (see Fig. 1). The properties of the gravitationally lensed objects and other candidate high- z lensed galaxies in this cluster are summarized in Table 2.

Lensing mass models with $\chi^2 < 1$ are found by fitting the ellipticity, orientation, center and mass parameters (velocity dispersion, core and truncation radii) of the cluster-scale component and the truncation radius and the velocity dispersion of the ensemble of cluster galaxies (using the scaling relations for early-type galaxies). The best estimates for these parameters are given in Table 3. In the

following we use mass estimates and redshift prediction from the galaxy cluster model built assuming a constant M/L for the individual galaxies. However, the predictions of the two models agree within the given errors.

In both mass models we find a small offset between the center of the cD galaxy and the cluster halo component. This is in agreement with recent findings by Covone et al. (2005), which have analyzed *Chandra* archive data and found an offset between the overall X-ray emission and the central galaxy of less than 1 arcsec.

Finally, the fiducial mass model has been used to derive constraints on the redshift of the other detected multiple images:

- 1) The very blue low surface brightness B1-B2 arc is predicted at $z = 1.25 \pm 0.05$, which is close to the photometric redshift derived for B1 ($z_{\text{ph}} \simeq 1.2$). In the VIMOS-IFU cube only a noisy spectrum of component the two sources could be detected, with no useful information to test the model prediction.
- 2) The blue pair C1-C2 shows a clear mirror symmetry on the HST images and is predicted to be located at $z = 1.6 \pm 0.1$. A possible identification of CIV in absorption would lead to $z = 1.578 \pm 0.002$ (flag = 1), very close to value predicted by the strong lensing model, but a higher S/N spectrum is needed in order to confirm the model's prediction.
- 3) Finally, the objects D1 and D2 are likely to be two images of the same object at $z = 3.2 \pm 0.2$. The model is predicting two other counter-images, all of them forming an Einstein cross, but we could not locate these additional 2 images as they are buried under the cD light. Unluckily, also for this system we could not identify any feature in the noisy VIMOS-IFU spectrum of this object that would have confirmed this redshift prediction, although this time the wavelength coverage was more adequate to search for the Lyman- α emission line. Therefore, this object has probably no strong Lyman- α emission line.

5.2. Comparison of cluster mass estimates

Our observations and analysis of this cluster allow us to constrain the mass of the cluster core using both dynamical and lensing mass estimates. Assuming a singular isothermal sphere model, the dynamical mass can be estimated using the relation (see, e.g., Longair 1998)

$$M(< R) = \frac{\pi \sigma^2 R}{G}. \quad (1)$$

Thus for a $30''$ radius ($R = 110 h_{70}^{-1}$ kpc), corresponding to the area covered by our spectroscopic survey, we derive a mass of $M = 7.1^{+3.1}_{-1.7} \times 10^{13} h_{70}^{-1} M_{\odot}$.

Although the mass within the gravitational arc radius is well constrained: $M(< 16'') = 2.9 \pm 0.1 \times 10^{13} h_{70}^{-1} M_{\odot}$, there is some weak degeneracies in the slope of the mass profile in the cluster core. Nevertheless, extrapolating to $110 h_{70}^{-1}$ kpc the lensing total mass is $7.2 \pm 0.2 \times 10^{13} h_{70}^{-1} M_{\odot}$, a value very close to the dynamical mass estimate.

While the present sample of redshift measurements does not allow a conclusive analysis of the whole cluster dynamical state, the present result supports the hypothesis that the cluster inner region is at hydrostatic equilibrium.

Assuming that the cluster follows the σ - T_X relation (e.g., Girardi et al. 1996), the ASCA observed X-ray temperature of $T_X = 5.95^{+0.42}_{-0.23}$ keV (Ota & Mitsuda 2004) corresponds to a velocity dispersion of 1000^{+190}_{-165} km s $^{-1}$, which is in good agreement with both our lensing and dynamical estimates. This also agrees with Allen et al. (1998) findings that galaxy clusters with centrally peaked X-ray emission and a short cooling time generally show a good agreement between lensing and X-ray mass estimates.

The agreement between the given dynamical and non-dynamical mass estimates further confirms that the core of A2667 is a relaxed system. Moreover, we note that the dynamical state of A2667 appears to be well predicted by its intra-cluster medium (ICM) temperature. Indeed, Cypriano et al. (2004) suggested that the ICM temperature is a good diagnostic for the dynamical state of a X-ray bright galaxy cluster: galaxy clusters with X-ray temperature below ~ 8 keV are likely to be relaxed systems, hence with a good agreement between dynamical and non-dynamical mass estimates (see also Cypriano et al. 2005).

However, we note that Allen et al. (2003) X-ray mass model, based on the more recent *Chandra* observations, under-predicts the size of the Einstein radius. Indeed converting the NFW parameters of their mass model fit into the Einstein radius for a $z = 1.0334$ source plane we found $\theta_E = 2.7$ arcsec, which is far from the observed 16 arcsec. This discrepancy is not surprising because of the small concentration ($c = 3$) of the NFW model. Indeed, keeping the same value of M_{200} , a value of $c = 5 - 6$ would match the $\theta_E = 16''$ measured. Not enough constraints close to the center lead to an overestimate of r_s and therefore to smaller values of the concentration c and the Einstein radius.

By combining strong and weak lensing Kneib et al. (2003) and Broadhurst et al. (2005) showed that NFW models with large concentration can match all lensing constraints. It is possible that a combined strong lensing and X-ray analysis would lead to similar results for A2667, although this is out of the scope of this paper.

Finally, we have determined the rest-frame K-band total light derived from the available ISAAC photometry as described in Section 5.1. Within the $110 h_{70}^{-1}$ kpc aperture, we found a luminosity of $L_K = 1.2 \pm 0.1 \times 10^{12} h_{70}^{-2} L_{\odot}$. Hence, we derived a M/L_K ratio of $61 \pm 6 h_{70} M_{\odot}/L_{\odot}$. This value is close to the $z \simeq 0$ values recently found by Rines et al. (2004), which have studied the M/L_K radial profile in a sample of nine nearby, X-ray luminous galaxy clusters. Within this sample, on the scale of $r \sim 250$ kpc, the measurements scatter in the range between 30 and 60 $h_{70} M_{\odot}/L_{\odot}$.

Table 3. Parameters of the two fiducial gravitational lensing models^a, assuming individual galaxies with $M/L=\text{const}$ and $M/L \propto L^{0.3}$, respectively. We list the offset between the cluster dark matter halo and the cD galaxy, the axis ratio, the orientation, the core radius, the velocity dispersion and the truncation radius. See text for details.

component	$\Delta R.A.$ (arcsec)	$\Delta Decl.$ (arcsec)	a/b	θ (deg)	r_{core} (kpc)	σ_v (km s ⁻¹)	r_{cut} (Mpc)
$M/L = \text{const.}$							
cluster halo	-1.6 ± 0.5	-0.5 ± 0.5	0.38	-45	74 ± 8	1004	1.3
L_* galaxy	–	–	–	–	(0.15)	130 ± 7	55 ± 10
$M/L \propto L^{0.3}$							
cluster halo	-0.8 ± 0.5	-1.8 ± 0.5	0.45	-45	76 ± 8	993	1.3
L_* galaxy	–	–	–	–	(0.15)	155 ± 8	70 ± 15

^a Quantities in parenthesis are not free parameters in the fit.

6. Conclusions

In this work we have presented the first integral field spectroscopic survey of a galaxy cluster performed with the VIMOS-IFU, together with a large set of broad band images of the same field. We have observed A2667, a massive, X-ray luminous galaxy cluster at $z = 0.233$, hosting one of the brightest gravitational arcs in the sky. We have obtained a spatially complete spectroscopic survey within the central $\simeq 100 h_{70}$ kpc. The redshift survey is complete down to $V_{606} \simeq 22.5$. We summarize our main findings here:

1. We have obtained spectroscopic redshift measurements for 34 sources, including 22 cluster members in the cluster core and the three images of the gravitational arc ($z = 1.0334$).
2. We have used the position and measured redshift of the giant arc A and the position and morphology of the multiple images B1-B2-B3, the extended triple object C1-C2-C3 and D1-D2 to build a strong gravitational lensing model of the matter distribution in the central $\sim 200 \times 200 \text{ kpc}^2$ around the cluster center. The strong lensing models derived using two different scaling laws for the cluster galaxy population ($M/L = \text{const}$ and $M/L \propto L^{0.3}$) give results which agree within the errors. The total mass within the Einstein radius ($r_E = 59.6 h_{70}^{-1} \text{ kpc}$) is $M(< 16'') = 2.9 \pm 0.1 \times 10^{13} h_{70}^{-1} M_\odot$, while the extrapolated value at $110 h_{70}^{-1} \text{ kpc}$ is $M = 7.2 \pm 0.2 \times 10^{13} h_{70}^{-1} M_\odot$, the error bar including the weak degeneracies in the slope of the mass profile. Moreover, the strong lensing models find a small offset between the dark matter halo and the position of the cD galaxy ($\Delta = 1.7 \pm 0.5 \text{ arcsec}$).
3. We have used the spectroscopic data for the dynamical analysis of the cluster core, and compared our mass estimates with the ones from recently published X-ray analysis. Within the radius $R = 110 h_{70}^{-1} \text{ kpc}$, the mass derived from the dynamical analysis is $M = 7.1^{+3.1}_{-1.7} \times 10^{13} h_{70}^{-1} M_\odot$, in very good agreement with the value from the strong lensing model. The velocity dispersion is found to be $\sigma = 960^{+190}_{-120} \text{ km s}^{-1}$, coher-

ent with the value derived from the observed X-ray temperature and assuming that the cluster follows the $\sigma - T_X$ relation. However, we caution that, although deep, our spectroscopic survey is confined to a limited linear region of the galaxy cluster, and a more extended redshift survey is warranted in order to define the dynamical status of the galaxy population of the cluster as a whole.

4. The published NFW mass model derived from X-ray measurement (Allen et al. 2003) finds a low value for the concentration c and can not account for the observed large Einstein radius. This is likely because of the lack of strong constraints in the cluster central region in the X-ray analysis. Indeed, recent studies of the lensing clusters ClG 0024+17 and A1689 (Kneib et al. 2003, Broadhurst et al. 2005), based on joint weak and strong lensing analyses, have demonstrated that large concentration NFW models are able to match all the observables.
5. Within a $110 h_{70}^{-1} \text{ kpc}$ radius, we find a rest-frame K-band M/L ratio of $61 \pm 5 h_{70} M_\odot/L_\odot$, as expected for an evolved stellar population and close to the value found for clusters in the local Universe.

The observed agreement between the dynamical and lensing mass estimates supports the idea that the cluster core is in a relaxed dynamical state, as expected from its regular X-ray morphology (Rizza et al. 1998, Allen et al. 2003) and its ICM temperature (Cypriano et al. 2004). Therefore, the core of A2667 appears to be dynamically evolved, in contrast with a large fraction ($70 \pm 20\%$) of similar X-ray luminous clusters at the same redshift ($z \sim 0.2$, Smith et al. 2005).

This work demonstrates the capabilities of wide f.o.v. integral field spectroscopy in obtaining spatially resolved spectroscopy of extended gravitational arcs and a complete (spatially and in magnitude) surveys of the galaxy population in the clusters cores at intermediate redshift. These measurements are useful in understanding the cluster mass distribution properties, using both the strong lensing and dynamical analyses. Wide field IFS is thus a

remarkable tool to probe compact sky regions such as the cluster cores targeted here.

Acknowledgements. The authors thank C. Adami, D. Grin, F. La Barbera, S. Brillant, G. Smith and D. Sand for useful comments and discussions, A. Biviano for providing an updated version of the program **ROSTAT**, and the anonymous referee for comments which helped in improving the presentation of the work. GC thanks his wife, Tina, for the enormous patience and invaluable support during all these years. The data published in this paper have been reduced using **VIPGI**, developed by INAF Milano, in the framework of the **VIRMOS** Consortium activities. GC thanks the **VIRMOS** Consortium team in Milano (B. Garilli, P. Franzetti, M. Scodreggio) for the hospitality during his stays at the IASF and the continuous help on the VIMOS-IFU data reduction. GC acknowledges support from the EURO-3D Research Training Network, funded by the European Commission under the contract No. HPRN-CT-2002-00305. JPK acknowledges support from CNRS and Caltech.

References

- Abell, G.O. 1958, *ApJS* 3, 211
- Allen, S.W. 1998 *MNRAS* 296, 392
- Allen, S.W., Schmidt, R.W., Fabian, A.C. et al. 2003, *MNRAS* 342, 287
- Beers, T.C., Flynn, K., & Gebhardt, K. 1990, *AJ* 100, 32
- Bertin, E. & Arnouts, S. 1996, *AAS* 117, 393
- Biviano, A. 2000, in *Constructing the Universe with Clusters of Galaxies, IAP 2000 meeting*, eds. F. Durret & D. Gerbal <http://nedwww.ipac.caltech.edu/level5/Biviano2/frames.html>
- Broadhurst, T., Takada, M., Umetsu, K. et al. 2005, *ApJ* 619, L143
- Caccianiga, A., Maccacaro, T., Wolter, A. et al. 2000, *AASS* 144, 247
- Campusano, L.E., Pelló, R., Kneib, J.-P. et al., 2001, *AA* 378, 394
- Condon, J.J., Cotton, W.D., Greisen, E.W. et al. 1998, *AJ* 115, 1693
- Covone, G., Adami, C., Durret, F. et al. 2005, submitted to *AA*
- Cypriano, E.S. et al. 2004, *ApJ* 613, 95
- Cypriano, E.S. et al. 2005, *ApJ* 630, 38
- D’Odorico, S. et al. 2003, *The Messenger* 113, 26
- Ebeling, H., Voges, W., Bohringer, H. et al. 1996, *MNRAS* 281, 799
- Ellis, R.S. et al. 2001, *ApJ*, 560, L119
- Egami, E., Kneib, J.-P., Rieke, G.H. et al. 2005, *ApJ* 618, L5
- Faber, S.M. & Jackson, R.E 1976 *ApJ* 204, 668
- Filippenko, A.V. 1982, *PASP* 94, 715
- Fruchter, A.S. & Hook, R.N. 2002, *PASP* 114, 144
- Fukazawa, Y., Makishima, K. & Ohashi, T. 2004, *PASJ* 56, 965
- Girardi, M., Fadda, D., Giuricin, G. et al. 1996, *ApJ* 457, 61
- Golse, G., Kneib, J.-P., Soucail, G. 2002, *AA* 387, 788
- Kassiola, A. & Kovner, I. 1993, *ApJ* 417, 450
- Kissler-Patig, M. et al. 2004, *AN* 325, 159
- Kneib, J.-P., 1993, PhD thesis, Université Paul Sabatier, Toulouse
- Kneib, J.-P., Ellis, R.S., Smail, I., Couch, W.J., Sharples, R.M., 1996, *ApJ*, 471, 643
- Kneib, J.-P., Hudelot, P., Ellis, R. S. et al. 2003, *ApJ* 598, 804
- Kneib, J.-P., van der Werf, P.P., Kraiberg Knudsen, K. et al., 2004a, *MNRAS* 349, 1211
- Kneib, J.-P., Ellis, R.S., Santos, M.R., Richard, J. 2004b, *ApJ* 607, 697
- Kurtz, M.J, Mink, D.J., Wyatt, W.F. 1992, *ADASS*, 1, 432
- Horne, K., 1986, *PASP*, 98, 609
- Jorgensen, I., Franx, M., Kjaergaard, P. 1996, *MNRAS* 280, 167
- Le Fèvre, O., Crampton, D., Lilly, S.J., Hammer, F., and Tresse, L. 1995, *ApJ* 455, 60
- Le Fèvre, O., Vettolani, G., Maccagni, D. et al. 2003, *The Messenger*, 111, 18
- Longair, M.S. 1998, *Galaxy Formation*, Springer-Verlag
- Lynds, R. & Petrosian, V. 1986, *BAAS* 18, 1014
- Natarajan, P. & Kneib J.-P. 1997, *MNRAS* 287, 833
- Navarro, J. F., Frenk, C. S., White, S. D. M., 1996, *ApJ* 462, 563
- Nolthenius, R. & White, S.D.M. 1987, *MNRAS*, 225, 505
- Ota, N. & Mitsuda, K. 2004, *AA* 428, 757
- Rizza, E., Burns, J. O., Ledlow, M. J. et al. 1998, *MNRAS* 301, 328
- Rines, K., Geller, M.J., Diaferio, A. et al. 2004, *AJ* 128, 1078
- Sánchez, S.F. 2004, *AN* 325, 167
- Saslaw, W. C. 1985, *ApJ* 297, 49
- Sand, D.J., Treu, T., Smith, G.P.; Ellis, R.S. 2004, *ApJ* 604, 88
- Sand, D.J., Treu, T., Ellis, R.S., Smith, G.P. 2005, *ApJ* 627, 32
- Santos, M.R., Ellis, R.S, Kneib, J.-P. et al. 2004, *ApJ* 606, 683
- Scodreggio, M., Franzetti, P., Garilli, B. et al. 2005, *PASP*, accepted (astro-ph/0409248)
- Smith, G.P., Kneib, J.-P., Smail, I. et al. 2005, *MNRAS* 359, 417
- Soucail, G., Fort B., Mellier, Y., Picat, J.P. 1987, *AA*, 172, L14
- Soucail, G., Mellier, Y. Fort, B. et al. 1988, *AA* 191, L19
- Soucail, G., Kneib, J.-P., & Golse, G. 2004, *AA* 417, L33
- Zanichelli, A., Garilli, B., Scodreggio, M. et al. 2005, *PASP*, accepted

Appendix A: Sensitivity and flux limits

While the VIMOS-IFU observations presented here were not meant for a blind search of pure emission-lines objects, it is anyway interesting to evaluate the sensitivity to faint high- z sources with no detectable continuum, i.e. the limiting flux above which a single emission-line would be detected in our datacube. See also Santos et al. (2004), for a similar discussion in a long-slit search for distant Ly- α sources.

In our datacube, an emission-line could be clearly detected if it covers at least 2 spatial elements and its total flux is 3 times the background root-mean-square fluctuations (i.e., the sky background noise) We considered a minimum spectral width of 3 lambda pixels, i.e. about the spectral resolution. We plot in Fig. A.1 the spatially averaged limiting flux of the whole VIMOS-IFU datacube as a function of the wavelength. At the edges of the spectral range, the main contribution comes from the worse sensitivity of the whole instrumental device (telescope, instrument, grism), while in the central regions, where the detection level is more uniform in wavelength, the limiting emission-line flux strongly depends on the atmospheric

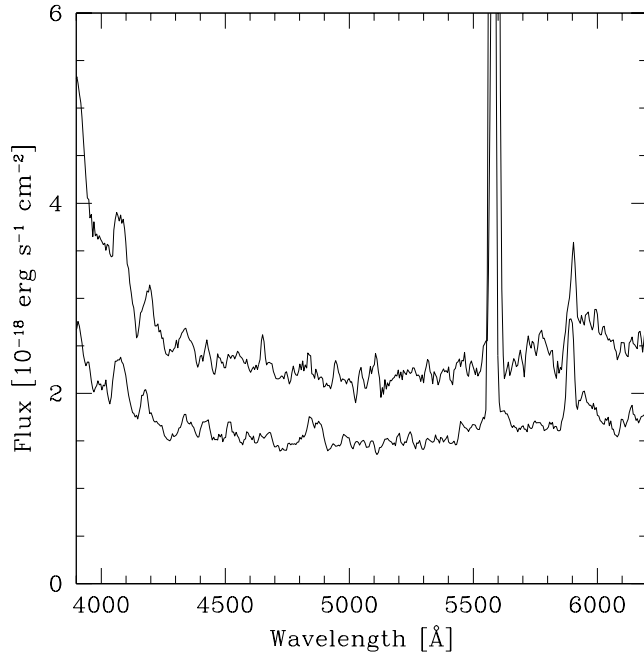


Figure A.1. The flux limits for the detection of emission lines sources in two different quadrants (Q1, upper curve, and Q2, lower curve) as a function of the wavelength. The curves for the other two quadrants fall between the two plotted here. See text for details.

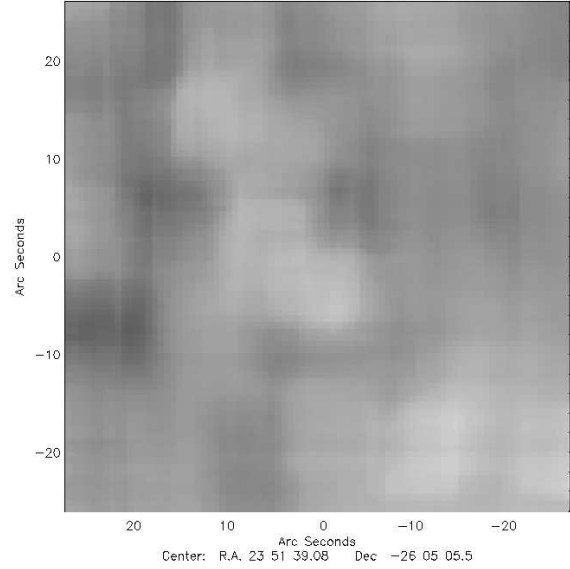


Figure A.2. 2D map of the sky background RMS, considering a window $\delta\lambda = 40 \text{ Å}$ wide at $\lambda = 5000 \text{ Å}$. A logarithmic scale from 10^{-19} to $10^{-18} \text{ erg cm}^{-2} \text{ s}^{-1} \text{ Å}^{-1}$ is used, with darker grey corresponding to lower sky levels.

OH airglow emission. In order to understand the spatial variations of the sensitivity, we show in Fig. A.2 a bi-dimensional map of the defined limiting emission-line flux at $\lambda \simeq 5000 \text{ Å}$.

We point out that the present observations were not conducted with the best strategy: an observational sequence of a larger number of dithered pointings with smaller exposition time would have been more effective in removing spatial not-uniformity, thus improving the final flux limit.